



Fe-complex of a tetraamido macrocyclic ligand: Spectroscopic characterization and catalytic oxidation studies

Shane Z. Sullivan^a, Anindya Ghosh^{a,*}, Alexandru S. Biris^b, Sharon Pulla^a, Anna M. Brezden^a, Samulel L. Collom^a, Ross M. Woods^b, Pradip Munshi^c, Laura Schnackenberg^d, Brad S. Pierce^{e,1}, Ganesh K. Kannarpady^b

^a Department of Chemistry, University of Arkansas at Little Rock, Little Rock, AR 72204, USA

^b University of Arkansas at Little Rock, Nanotechnology Center, Little Rock, AR 72204, USA

^c Reliance Industries Limited, Research Center, Vadodara, India

^d National Center for Toxicological Research, Jefferson, AR 72079, USA

^e Department of Chemistry and Biochemistry, The University of Texas at Arlington, Arlington, TX 76019-0065, USA

ARTICLE INFO

Article history:

Received 29 June 2010

In final form 1 September 2010

Available online 6 September 2010

ABSTRACT

This work presents the spectroscopic characterization and reaction studies of a Fe^{III}-complex (**2**) of a tetraamido macrocyclic ligand (**1**, 15,15-dimethyl-5,8,13,17-tetrahydro-5,8,13,17-tetraaza-dibenzo[a,g]cyclo-tridecene-6,7,14,16-tetraone). **2** was characterized primarily by means of EPR. In agreement with the magnetic moment ($\mu_{\text{eff}} = 3.87 \text{ BM}$), EPR spectroscopy of **2** shows signals consistent with $S = 3/2$ intermediate-spin ferric-iron. Besides EPR, mass spectrometry, UV/vis spectroscopy and cyclic voltammetry were used to further characterize **2**. **2** is soluble in water and activates hydrogen peroxide under ambient conditions. **2** catalytically bleaches dyes, pulp and paper effluents and oxidizes several amines to their corresponding N-oxides with high turnover number and good yields.

© 2010 Elsevier B.V. All rights reserved.

1. Introduction

Annually, several tons of hydrogen peroxide (H₂O₂) [1,2] are used for industrial oxidation purposes. By itself, H₂O₂ is a reasonably moderate oxidant but its oxidizing activity can be significantly enhanced by variety of metal complexes. The major challenge in the design of H₂O₂-activating catalysts is selecting a suitable metal ligand which can stabilize high-valent metal oxidation states while simultaneously remaining resistant to self-oxidation [3]. With this caveat in mind, a major research effort has evolved which focuses on biologically inspired metal complexes mimicking the structures and function of H₂O₂ or oxygen (O₂) activating metalloenzymes [4–8]. Generally speaking, this is accomplished by carefully controlling the geometry of the metal coordination site and the electron donating ability of the ligand(s) to modulate the H₂O₂- or O₂-activating capacity of the catalyst. In recent years various metal complexes have been investigated, each employing a myriad of donor ligands to effectively catalyze either O₂- or H₂O₂-dependent oxidation reactions [1,9–16]. Among these catalysts, a series of H₂O₂-activating iron-complexes developed by Collins and co-workers is particularly noteworthy as ‘green catalysts’ for performing various

oxidations [3,17] in water. These complexes utilize a tetraamido macrocyclic ligand to coordinate a mononuclear ferric-iron.

Ellis et al. [18] recently reported a new generation of tetraamido macrocyclic ligands and their Fe^{III}-complexes including ligand **1** and complex **2** (Figure 1). The iron-complexes were found to be highly active in activating H₂O₂ rapidly in aqueous solutions in the pH range of 7–9 and subsequently tested for dye bleaching (Orange II). However, reactions of **2** were limited only to bleaching of one water soluble dye as reported by the authors. This has made us curious to study the Fe-complex additionally for various oxidations. Beside this, spectroscopic characteristics such as ESI-MS, EPR, UV/vis spectroscopy, cyclic voltammetry, and magnetic susceptibility of **2** provided us additional scope for investigating **2** in terms of further characterizing the Fe-complex. Therefore, the work presented here describes the bleaching of pulp and paper effluents, various water soluble organic dyes and synthesis of N-oxides from their corresponding amines along with detailed spectroscopic investigation of the Fe^{III}-complex containing the new variant of the tetraamido macrocyclic ligands (**1**, Figure 1) which were not studied previously.

As compared with other tetraamido macrocyclic ligands, the synthesis of **1** is much simpler and economic and does not require the use of an amino acid starting material [18]. This Fe^{III}-oxalamide complex (**2**, Figure 1) was found to be amenable to physicochemical characterization by ESI-MS, UV-visible, EPR spectroscopy, cyclic voltammetry, and magnetic susceptibility. Furthermore,

* Corresponding author. Fax: +1 501 569 8838.

E-mail address: axghosh@ualr.edu (A. Ghosh).

¹ Equal work was contributed by these authors.

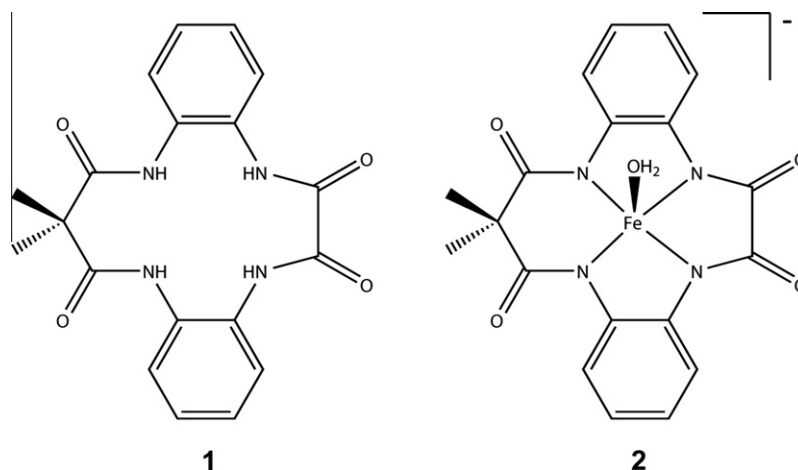


Figure 1. Tetradentate amidomacrocyclic ligand (**1**) and its Fe-Complex (**2**). The counter cation is not shown.

catalytic studies of **2** using H_2O_2 as a primary oxidant are provided. In these experiments **2** rapidly catalyzes the H_2O_2 -dependent oxidation of various water soluble organic dyes and paper pulp effluent under mild reaction conditions and ambient temperature. **2** also behave as a catalyst for the synthesis of small organic N-oxides from their corresponding organic amines. These results demonstrate the overall chemical versatility of tailored tetraamido macrocyclic ligands for a variety of industrial applications.

2. Experimental

2.1. Materials and methods

All chemicals, reagents, and solvents were obtained either Sigma–Aldrich (USA) or Fisher Scientific (USA) and used without further purifications unless otherwise noted. Tetrahydrofuran (THF) was purified using sodium metal and benzophenone. ^1H NMR spectra were obtained using a 600 MHz Bruker Avance instrument equipped with a 5 mm triple resonance inverse probe. Infrared (IR) spectra were obtained using a Nicolet Magna IR 500 spectrometer. Electrospray ionization mass spectra (ESI-MS) were obtained using an Applied Biosystem API-4000 spectrometer or using an Agilent 100 series MSD VL spectrometer. Gas Chromatography Mass spectra (GC/MS) were obtained using an Agilent G1701DA GC/MSD. UV–visible spectroscopy was performed using a Varian Cary 5000 UV–visible-NIR spectrophotometer. Electrochemical studies were performed using a Pine Instrument Company Biopotentiostat (model no. AFCBP1). Elemental analysis was performed at Midwest Microlab LLC., Indianapolis. Magnetic susceptibility was measured using Alfa Aesar magnetic susceptibility balance-mark 1.

Section 2 for bleaching studies, N-oxide synthesis, cyclic voltammetry, and demetallation study are given in the [supporting information](#).

2.2. Electron paramagnetic resonance (EPR) spectroscopy

X-band (9 GHz) EPR spectra were recorded on a Bruker EMX Plus spectrometer equipped with a bimodal resonator (Bruker model 4116DM). Low-temperature measurements were made using an Oxford ESR900 cryostat and an Oxford ITC 503 temperature controller. A modulation frequency of 100 kHz was used for all EPR spectra. All experimental data used for spin-quantitation were collected under non-saturating conditions. EPR spectra were simulated and quantified using Spin Count (ver.3.0.0), created by Professor M.P. Hendrich at Carnegie Mellon University. The

spectral line-width is dominated by *D* and *E*-strain. Therefore simulations employ GAUSSIAN distributions in the *D*-values and the ratio of *E/D* to produce the correct line-width, specified as σ_D and $\sigma_{E/D}$, respectively. Least squares and deconvolution analysis of the spectra were combined to allow relevant parameters to vary while maintaining a sum of multiple species that best-fit the experimental data. The simulations were generated with consideration of all intensity factors, both theoretical and experimental, to allow concentration determination of species. The only unknown factor relating the spin concentration to signal intensity was an instrumental factor that depended on the microwave detection system. However, this was determined by the spin standard, Cu(EDTA), prepared from a copper atomic absorption standard solution purchased from Sigma–Aldrich.

The half-power microwave saturation ($P_{1/2}$) was determined by least-squares fitting the intensity of the derivative signal (*I*) as a function of microwave power (*P*) using Eq. (1). The variable *b* is an inhomogeneity factor which varies between 1.0 for inhomogeneous and 3.0 for homogeneous line broadening.

3. Results and discussion

3.1. Preparation of catalyst **2**

Synthesis of **2** was performed according to the method reported by Ellis et al. with minor modifications [18]. The synthetic details for both **1** and **2** are described in the [supplementary information](#).

3.2. Electron spray ionization mass spectrum (ESI-MS)

If the iron within **2** has a +3 oxidation state, the resulting complex would be monoanionic and thus observable in the negative ion mode when analyzed by ESI-MS. Indeed, as observed in [Figure 2](#) the ESI-MS spectrum of **2** has a pronounced peak at 418 m/z. Moreover, the theoretical isotopic distribution shown within the inset of [Figure 2](#) is consistent with the experimentally observed isotope distribution. Taken together, these results support the formation of the ferric-iron complex shown in [Figure 2](#). Elemental analysis was performed to confirm the expected elemental composition of the desired product.

While the axial water ligand indicated in the [Figure 1](#) could not be observed by ESI-MS it is possible that this labile ligand is dissociated within the harsh conditions of the mass spectrometer. In fact, an axial water ligand was observed in the X-ray crystallographic structure of analogous Fe-tetraamido macrocyclic ligand

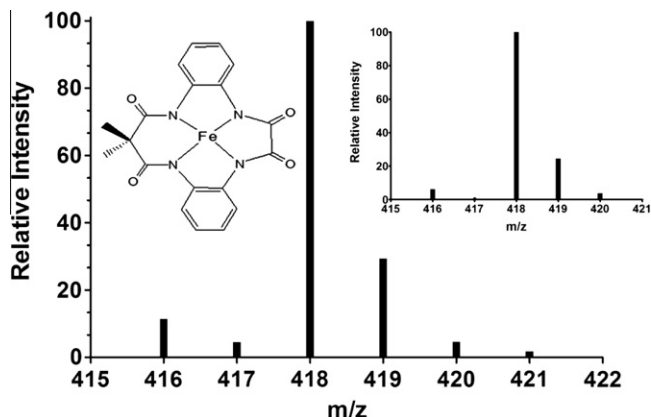


Figure 2. ESI-MS of Fe-Complex (2) and its theoretical isotope distribution (inset).

complexes [18,19]. Furthermore, as will be discussed in greater detail below, the EPR spectra of **2** is similar to analogous Fe^{III}-tetraamido macrocyclic ligand complexes in the presence of an axial aqua- or hydroxo-ligand. Therefore the presence of an axial water ligand on **2** cannot be completely ruled out at this point.

3.3. UV-visible spectroscopy and electrochemical studies

Figure S3 (supporting information) shows the UV-visible spectra of **1** and **2** dissolved in acetonitrile. Ligand **1** is a white solid and thus is not expected to exhibit any peaks within the visible range. Within the UV region a single peak is observed at 202 nm with a shoulder at 223 nm. Alternatively, complex **2** is a dark red solid and thus exhibits several absorption features within the visible spectrum (268, 346 nm, and a relatively weak but broad shoulder at 500 nm). The molar extinction coefficient at 450 nm ($4050 \text{ M}^{-1} \text{ cm}^{-1}$) was used for quantitative purposes. As discussed below, both EPR spectroscopy and magnetometry confirms the oxidation state of **2** is ferric. The bands within the visible region are largely attributable to ligand to metal charge transfer bands. However, the lower extinction coefficient ($\epsilon \sim 500 \text{ M}^{-1} \text{ cm}^{-1}$) observed for the features above 400 nm could be from $d-d$ transitions within an intermediate-spin d^5 -ion assuming tetragonal distortion.

The cyclic voltammetry of **2** was performed in acetonitrile containing 0.1 M *n*-tetrabutylammonium hexafluorophosphate as electrolyte with respect to Ag/AgCl electrode at 298 K. As illustrated in Figure S3 (supporting information), the voltamogram for **2** exhibits one peak at $E_{1/2} = 0.50 \text{ V}$ ($\Delta E_p = 100 \text{ mV}$) within the potential range of 0.2–1 V. Previous Fe^{III}-tetraamido macrocyclic ligand complexes show peaks within the $E_{1/2}$ -range of 0.44–1.0 V. The broad range of redox potentials available for Fe^{III}-tetraamido macrocyclic ligand complexes is largely a result of substitution of electron donating or withdrawing functional groups on the tetraamido macrocyclic ligand backbone [20]. For example, Fe-tetraamido macrocyclic ligand complex without any modification on the benzene ring exhibit a redox potential of $E_{1/2} = 0.76 \text{ V}$ where as with Fe-tetraamido macrocyclic ligand with dimethyl substitution on the benzene ring shows $E_{1/2} = 0.44 \text{ V}$ [20]. By analogy, the peak observed at $E_{1/2} = 0.50 \text{ V}$ for complex **2** can be similarly assigned a one electron oxidation for a Fe^{III}/Fe^{IV} couple. However, while unlikely, the possibility that a Fe^{III} radical cation or a dimeric species is being produced cannot be completely ruled out.

3.4. Electron paramagnetic resonance spectroscopy

The initial EPR characterization of complex **2** was complicated by the tendency of this molecule to form intermolecular aggregates

in acetonitrile (ACN) at high concentrations (1–2 mM). While this phenomenon was not observed in UV-visible, electrochemical, or kinetic studies, the working concentration for typical EPR experiments is several orders of magnitude higher. As a result, EPR spectra of **2** in ACN show only weak ($S = 3/2$) signals typically observed for Fe^{III}-tetraamido macrocyclic ligand complexes. Furthermore, as observed in Figure 3, at elevated temperature (above 50 K) a broad signal can be seen at $g \sim 2.3$. As indicated by the inset (Figure 3), the signal at $g \sim 2.3$ does not follow Curie-law behavior as in that its intensity increases quadratically with temperature. This quadratic response to increased temperature is not consistent with a change in the Boltzmann population of a well defined spin-manifold, and therefore cannot be attributed to a simple dimeric or multimeric molecular aggregate of complex **2**. Moreover, as indicated by the dashed lines (Figure 3), this resonance is initially observed at $g \sim 2.6$ at temperatures below 50 K. However, at temperatures above 50 K, the resonant position for this signal shifts up-field to $g \sim 2.3$. Taken together, these observations are consistent with a signal originating from superparamagnetic relaxation of ferric nanoparticles, likely from aggregation of complex **2** in ACN [21–24]. The line shape and temperature dependence for this class of paramagnetic signals are highly dependent on the size, geometry, and composition of the nanoparticles, therefore no meaningful interpretation can be made regarding these spectra. For this reason several glassing solvents and glassing mixtures were evaluated to prevent aggregation of complex **2** in frozen samples [25]. The aggregation of the iron complex (**2**) at high concentration in ACN is due to the unique nature of the ligand (**1**). The ligand (**1**) is much less sterically hindered compared to previously reported tetraamido macrocyclic ligands [3,17] and as a result metal complexes (**2**) can come close to each other to form aggregates presumably via either a water or hydroxo bridge. Unlike ligand **1**, conventional tetraamido macrocyclic ligands [3,17] contain several methyl groups which render the ligands and their corresponding iron-complexes

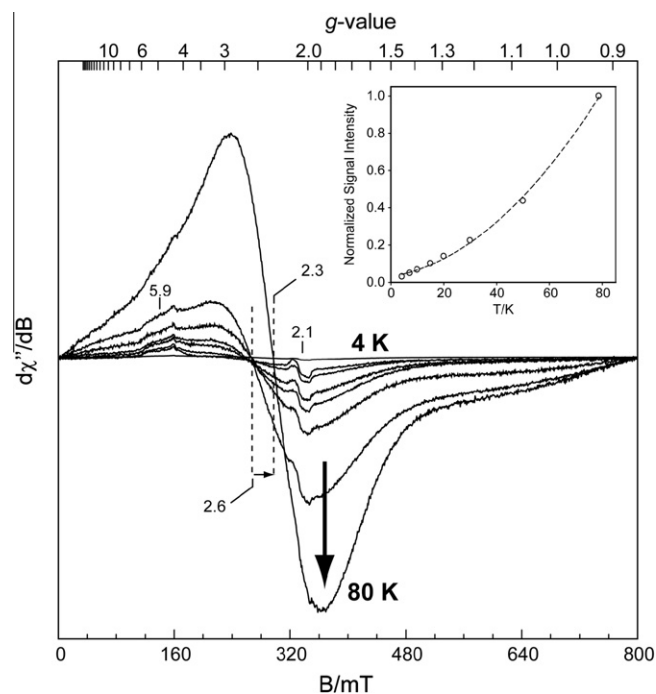


Figure 3. Temperature dependent X-band EPR spectra of 1.32 mM complex **2** in pure acetonitrile. Selected EPR spectra were collected at 4, 7, 10, 15, 20, 30, 50, and 80 K and are normalized to correct for Curie-law dependence. (Inset) Normalized signal intensity of the $g \sim 2.3$ features with increasing temperature. A simple quadratic function (dashed line), $y = y_0 + ax + bx^2$ is overlaid on the data for clarity.

more sterically hindered and results in less or almost no aggregation.

By altering the solvent composition from pure ACN to a 1:1 mixture of toluene/ethanol nearly all indications of molecular aggregation (as observed by EPR spectroscopy) were eliminated. As illustrated in Figure 4 the 10 K EPR spectra (solid line, **I**) of complex **2** (in 1:1 toluene/EtOH) shows signals consistent with a ferric-iron in an intermediate axial-ligand field, $S = 3/2$ [26,27]. Based on the effect of the solvent on the EPR spectra it is possible that EtOH is acting as an axial ligand to the Fe-tetraamido macrocyclic ligand complex. This could potentially decrease molecular aggregation via a bridging water or hydroxide ligand.

The temperature dependence, microwave power saturation behavior, and spectral features associated with spectra **I** can only be understood if the observed EPR spectra is fit to two spectroscopically distinct $S = 3/2$ species, termed **2a** and **2b** henceforth. A quantitative component sum simulation (dashed line, **SI**) for the spectra associated with species **2a** and **2b** was utilized to generate the simulation **SI** for complex **2**. Species **2a** is the dominate component of EPR spectra **I** representing 86% of the total $S = 3/2$ species observed by EPR spectroscopy. The signals observed at g -values of 4.67, 4.18, and 1.88 originate from a transition within the $m_s = 1/2$ doublet of the $S = 3/2$ spin-system with an E/D -value of 0.15. Similar signals have been previously observed in Fe-tetraamido macrocyclic ligand complexes with one axial water ligand and one axial hydroxide ligand [19].

The EPR line-width of **2b** is dominated by g -anisotropy and E/D -strain which is consistent with other ferric-tetraamido macrocyclic ligand complexes [19]. The increased rhombicity of this species allows for significant mixing of the $m_s = 1/2$ and $3/2$ -eigenstates. As a

result, the intensity of the transition within the $m_s = 3/2$ doublet observed at $g = 5.89$ shows significant intensity. As discussed previously, it was not possible to observe the axial ligand as suggested for the complex **2**. However based on the EPR signals with g -anisotropy and E/D -strain of the complex **2** and observing the similarity of the EPR signal of previously reported similar complexes [19], the existence of the axial ligand(s) in the complex **2** can be surmised.

Upon correction of the observed signals for Curie-law dependence, the observed signal intensity of these transitions is inversely correlated as a function of temperature. Thus the intensity of the $g = 5.89$ signal is greatest at lower temperature whereas the signal observed at $g = 4.67$ increases with temperature. The assignment of these features are further corroborated by fitting the temperature-normalized signal intensity to a Boltzman population distribution for a 2-level system; Figure 5A(○), (solid line). From the best-fit to each transition, the value for the axial-zero field splitting term (D) for **2a** was determined to be $D = -1.9 \pm 0.2 \text{ cm}^{-1}$. Thus the $m_s = 3/2$ doublet represents the ground state of the **2a** $S = 3/2$ spin-system.

Species **2b** represents a minority fraction of EPR spectra **I** representing only 14% of the total $S = 3/2$ species. This component shows considerably less g -anisotropy and a more axial magnetic symmetry, E/D -value of 0.07. Given the low concentration of this species it could easily be overlooked. However, the sharp spectral features observed in spectra **I** at $g = 4.35$ and 1.99 cannot be simulated within **SI** while simultaneously maintaining the features associated with **2a** at $g = 5.89$ and 4.67. As observed in Figure 3, the signal intensity observed at $g = 1.99$ is largely dominated by species **2b**, and very little intensity originates from **2a** due to its broad features within this region of the spectrum. Conversely, the signal intensity observed at $g = 4.67$ (and 5.89) is nearly completely attributed to species **2a**. As illustrated by Figure 5A, the temperature dependence of the feature at $g = 1.99$ associated with **2b** is significantly different than that observed at $g = 4.67$ for **2a**. Since there are only two doublet within a $S = 3/2$ spin-system, these two spectroscopic features cannot be attributed to the same $S = 3/2$ species. As illustrated in Figure 5A(●), (dashed line), the same procedure outlined for **2a** can be used to determine the D -value for **2b**; $D = -3.6 \pm 0.3 \text{ cm}^{-1}$. While the magnitude of the **2b** D -value is significantly larger than that of **2a**, both species have a ground state $m_s = 3/2$ doublet.

The microwave power saturation behavior of **2a** and **2b** was determined at 10 K as a final confirmation for the presence of two species. As with the temperature dependence, the signal intensity as a function of microwave power shown in Figure 5B was measured at $g \sim 4.67$ for **1a** and $g = 1.99$ for **2b**. The half-saturation microwave power ($P_{1/2}$) for species **2a** and **2b** was determined by least-squares fit to Eq. (1) [28,29].

$$\log(I/\sqrt{P}) = \log I_0 - b/2 \times \log(1 + p/p_{1/2}). \quad (1)$$

Within this temperature regime the line-width of **2a** and **2b** are not significantly broadened as a function of temperature and thus both species exhibit inhomogeneous saturation behavior ($b = 1$) and are best-fit to a $P_{1/2}$ -value of 85 ± 10 and 40 ± 5 mW, respectively. Given the additional spectral feature observed at $g = 5.89$ for **2b** and the differential temperature dependence and microwave saturation behavior observed at $g = 4.67$ and $g = 1.99$, the observed EPR spectra **I** can be quantitatively simulated using two spectroscopically distinct $S = 3/2$ species, **2a** and **2b**.

The $S = 3/2$ spin-state observed for **2a** and **2b** is consistent with the magnetic moment ($\mu_{\text{eff}} = 3.87$ Bohr Magneton) determined by the Gouy method. This value for the spin-only magnetic moment is consistent with three unpaired electrons, $S = 3/2$. Furthermore, as stated in the Section 2, the concentration of each species was

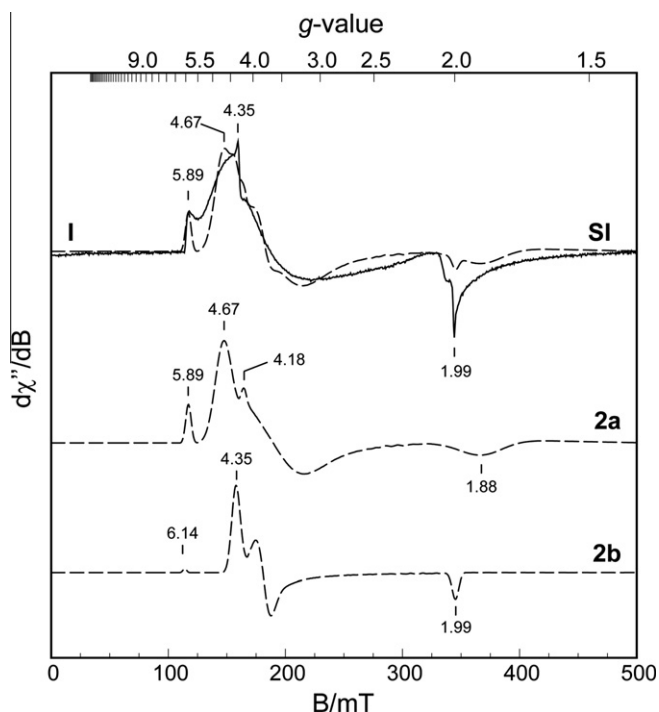


Figure 4. X-band EPR spectra (solid line) of 1.0 mM complex **2** at 10 K in 1:1 (toluene:EtOH). A component simulation for the spectra associated with species **2a** and **2b** was utilized to generate the simulation (dashed line, **SI**). Using this technique, the relative concentration for species **2a** and **2b** was determined by least-squares analysis to be 86% mM and 14%, respectively. Instrumental parameters: microwave frequency, 9.64 GHz; microwave power, 0.63 mW; modulation amplitude, 0.92 mT; temperature, 10 K. Simulation parameters: (**2a**) $S = 3/2$; $g_{xyz} = 2.28, 1.95, 2.01$; $\sigma_{g_{xyz}} = 0.03$; $D = -1.90 \text{ cm}^{-1}$; $\sigma_D = 0.04 \text{ cm}^{-1}$; $E/D = 0.15$; $\sigma_{E/D} = 0.05$; $\sigma_B = 1.5 \text{ mT}$; (**2b**) $S = 3/2$; $g_{xyz} = 2.11, 2.00, 2.02$; $D = -3.60 \text{ cm}^{-1}$; $E/D = 0.07$; $\sigma_{g_{xyz}} = 0.02, 0.03, 0.004$; $\sigma_D = 0.6 \text{ cm}^{-1}$; $\sigma_{E/D} = 0.02$; $\sigma_B = 1.5 \text{ mT}$.

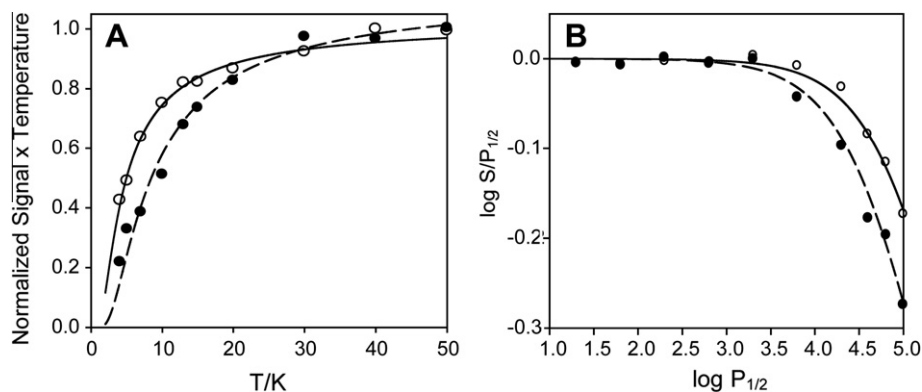


Figure 5. A. Normalized temperature dependence of $S = 3/2$ species **2a** (○) and **2b** (●). The values for the axial-zero field splitting term (D) for each species (**2a**, $D = -1.9 \pm 0.2 \text{ cm}^{-1}$; **2b**, $D = -3.6 \pm 0.3 \text{ cm}^{-1}$) were determined by fitting the data to a Boltzman-dependent population distribution for a 2-level system. B. Microwave power saturation behavior of the two $S = 3/2$ species **2a** (○) and **2b** (●) at 10 K. The half-saturation microwave power ($P_{1/2}$) for species **2a** and **2b** were determined by least-squares regression according to published methods.^{22, 23} Within this temperature regime the line-width of **2a** and **2b** are not significantly broadened as a function of temperature and thus both species exhibit inhomogeneous saturation behavior ($b = 1$) and are best-fit to a $P_{1/2}$ -value of 85 ± 10 and 40 ± 5 mW, respectively.

determined by component simulation. Using this approach the concentration of species **2a** and **2b** within sample **I** (Figure 3) was determined to be 0.61 and 0.10 mM, respectively. This value represents $\sim 71\%$ of the total iron in the sample as determined by UV–visible spectroscopy.

3.5. Stability of the complex

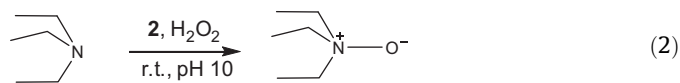
Experimental sections are given in the supporting information. The complex is stable in neutral to alkaline aqueous solutions for several days at moderately high temperature (40–50 °C). However, heating the aqueous solutions of **2** to 90 °C causes the catalyst to demetallate rapidly as indicated by changes in the UV–visible spectra (Figure S5, supporting information). Demetallation gives rise to the free ligand, which was verified by ¹H NMR. This is a limitation of using **2** at very high temperature. Macrocyclic ring size and amide planarity are critical for hydrolytic stability of iron-complexes of deprotonated amide ligands. The Fe-complex of a tetra-amido macrocyclic ligand with a ring size of fourteen atoms was found to be extremely unstable in water [19]. With this in mind, **2** was synthesized with a ring size of thirteen atoms with the intention that this size should provide adequate stability to the Fe-complex in aqueous solution. However, the instability of the complex at high temperature is not currently understood. One potential explanation for the thermal instability of **2** may be attributed to the increased rigidity of this complex. Unlike other Fe–TAML complexes, **2** has two aromatic rings which makes the complex very rigid and thus may decrease the strength of the ligand chelation to the iron ion.

3.6. Oxidation studies

Experimental sections are given in the supporting information. Textile industries produce a large quantity of water effluent which requires treatment to remove colored compounds prior to release. Activated H₂O₂ provides an effective and inexpensive means to treat water effluent. For this purpose the catalytic efficiency of complex **2** as an activator of H₂O₂ was evaluated by UV–visible spectroscopy. In these experiments orange IV (**a**), clayton yellow (**b**), methyl orange (**c**), methyl violet (**d**), and naphthol B green (**e**) were used as a substrate-surrogate to illustrate the efficacy of **2** catalyzed H₂O₂-bleaching within an aqueous CO₃²⁻/HCO₃⁻ buffer (pH 10) [30]. As a control, one dye (**f**, Orange IV) was monitored in the absence of **2**. Figure 6A shows the relative change in absorbance for each dye (12 μM) at the wavelength specified in Table 1

in the presence of catalytic amounts of **2** (0.5 μM). The reaction was initiated by addition of H₂O₂ to a final concentration of 3 mM. A small amount (10 ppm) of ethylenediamine tetraacetate (EDTA) was added to each reaction mixture to minimize Fenton-based hydroxyl radical chemistry associated with free transition metals. As indicated by Figure 6A the bleaching for all dyes showed nearly complete bleaching within 9-min at ambient temperature. The rate of dye bleaching was measured at both pH 10 and 11.5 to demonstrate the tolerance of **2** under basic conditions. As illustrated in Table 1 the bleaching time for each dye is essentially the same at pH 10 and 11.5 indicating the efficacy of **2** within this pH range. The deviations observed in the rate of dye bleaching catalyzed by **2** can likely be attributed to differences in the nature and accessibility of oxidizable groups in each dye. For example, H₂O₂-dependent bleaching of Methyl Orange by **2** was considerably slower than observed for other organic dyes. However, dye bleaching by H₂O₂ alone under similar conditions shows no bleaching within the time observed (15-min). As with previously reported Fe–TAML catalysts complex **2** is slowly inactivated under multiple turnover conditions resulting in decreased bleaching efficiency [30].

The ability complex **2** to catalyze H₂O₂-dependent bleaching of paper pulp and paper effluent was directly measured spectrophotometrically using a similar procedure as for dye-bleaching studies. In these experiments 6 mg of catalyst **2** was added per liter of effluent and the absorbance was monitored at 466 nm for 4 h upon addition of 28.2 mM H₂O₂ at pH 9.5 [31,3]. As shown in Figure 6B, under these conditions complex **2** (13 μM) decreased the absorbance by 52% within 4 h at ambient temperature. While H₂O₂ alone is also capable of bleaching paper pulp effluent under similar conditions, the rate and extent of bleaching is significantly lower than observed for **2** catalyzed bleaching. The rates observed here for dye bleaching are consistent with the kinetic findings recently reported by Ellis et al. [$1-10 \times 10^5 \text{ M}^{-1}\text{s}^{-1}$] [18].



In addition to the bleaching of organic dyes and paper effluents, complex **2** was evaluated as a synthetic catalyst to oxidize a variety of tertiary amines to their corresponding N-oxides (Eq. (2)). This simple oxidation chemistry is remarkably useful for both synthetic and biological applications [32,33]. In all instances these reactions were performed at room temperature and pH 10. After 2 h each reaction was quenched and products analyzed by GC/MS as

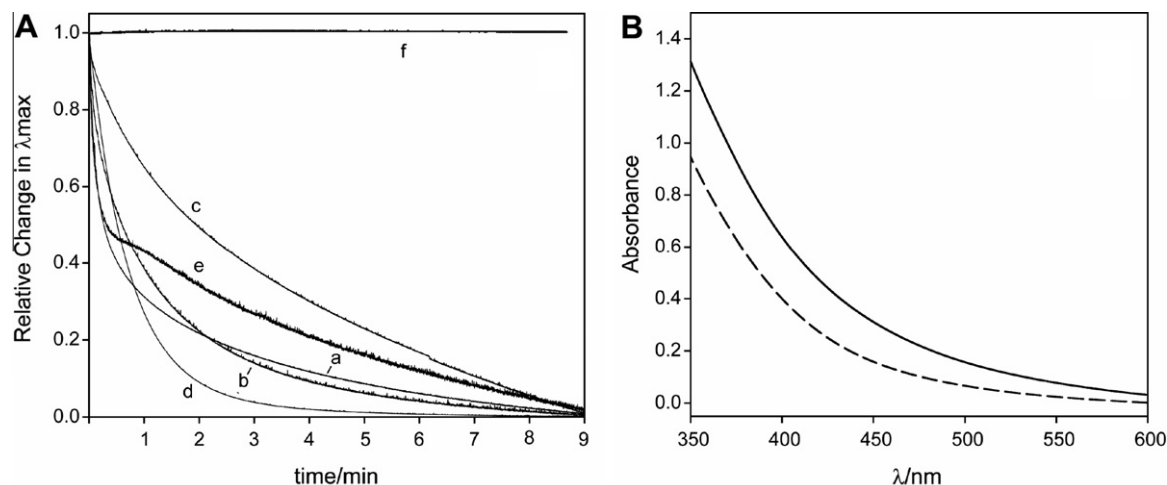


Figure 6. A. The rate of bleaching for the water soluble dyes listed in Table 1. Each dye was monitored by UV–visible spectroscopy at its corresponding absorption maximum. Reaction conditions: temperature, 25 °C; 10 ppm EDTA; pH 10; 12 μ M dye; 31.3 mM H_2O_2 ; and 0.5 μ M catalyst **2**. B. Room temperature bleaching of paper pulp effluent following treatment with 13 μ M **2** and 28.2 mM H_2O_2 for 4 h at 25 °C.

Table 1
Dye bleaching reactions using **2** in H_2O .

Entry	Dye	λ_{max}^a (nm)	Bleaching time ^b	
			pH 10 (s)	pH 11.5 (s)
a/f	Orange IV	444	310	305
b	Clayton yellow	403	307	295
c	Methyl orange	464	>600	>600
d	Methyl violet	584	235	225
e	Napthol B Green	718	325	335

^a λ_{max} was the wavelength used to determine bleaching time.

^b Bleaching time is defined to be the time required for the absorbance to reach half its initial value.³⁰ All reactions performed in pH 10 or 11.5 carbonate buffer with 10 ppm EDTA, dye concentration of 12 μ M, H_2O_2 concentration 31.3 mM, and catalyst (**2**) concentration of 0.5 μ M at 25 °C. As a control the bleaching of Orange IV by H_2O_2 in the absence of catalyst **2** (f) is shown in Figure 6.

described within the Section 2. As shown in Table 2 the reactions catalyzed by **2** show yields approaching stoichiometric conversion in some instances. The catalytic efficiency of **2** was determined by the number of moles of product produced per mol of catalyst. For clarity, this ratio is termed the turnover number (TON) henceforth. For the amines selected (Table 2), the TON observed for **2** range from 404 to 608. Among several amines triethylamine showed the highest reactivity to form the N-oxide followed by N,N-diisopropylamine and N,N-diethylaniline. Understandably, these amines are relatively easy to oxidize thus resulting in the high yields and TON observed. Pyridine and N,N-diisopropylethylamine

Table 2
N-oxide formation of amines catalyzed by **2**^a.

Entry	Amine	TON	Yield ^b
1	N,N-diisopropylethylamine	415 \pm 50	40.2 (0)
2	N,N-diisopropylamine	514 \pm 51	49.7 (0)
3	N,N-dimethylaniline	481 \pm 36	46.5 (15.8)
4	N,N-diethylaniline	468 \pm 54	45.3 (18.9)
5	Triethylamine	608 \pm 83	58.8 (0)
6	Pyridine	404 \pm 20	39.1 (22.9)
7	4-dimethylaminopyridine ^c	–	–

^a All the reactions were performed at room temperature at pH 10 in carbonate buffer. H_2O_2 was added as a primary oxidant for all reactions. Product yield was determined after 2 h.

^b Values in parenthesis indicate % yields of N-oxides by hydrogen peroxide only.

^c Product formation was not quantified.

were found to be the less reactive substrates to furnish N-oxides in lower yields (39–40%) and lower turnover numbers (404–415) due to the difficulty in oxidizing these amines. Both steric and electronic factors must be considered in order to justify the difference in reactivity of various amines. Alternatively, reactions carried out in the absence of **2** and using only H_2O_2 as a primary oxidant resulted in nearly no (or very little) N-oxide product formation. These results demonstrate the versatility of **2** and its ability to activate H_2O_2 under relatively mild reaction conditions. Free metal ions are also known to catalyze oxidation reactions [34], but that is not the case here as reactivity will drop dramatically if free metal ion in such low concentration is the sole reactive species.

4. Conclusion

In this work a water soluble Fe-tetraamido macrocyclic ligand complex was synthesized and characterized by UV–visible, EPR spectroscopy, magnetometry, and ESI-MS. The synthesis of this Fe-complex is relatively straight forward and can be produced in large quantities. EPR spectroscopy reveals two spectroscopically distinct forms of this complex, termed **2a** and **2b**. The heterogeneity of complex **2** observed by EPR spectroscopy can likely be attributed to differential protonation states of one or both axial water ligands. In agreement with magnetic susceptibility measurements complex **2** exhibits an $S = 3/2$ spin-state consistent with ferric-iron within a strong-axial-ligand field. As a cautionary note, complex **2** showed a propensity for molecular aggregation at concentrations amenable to spectroscopic characterization. Therefore, some care should be employed in the selection of an appropriate solvent system prior to future spectroscopic investigation of reactive intermediates.

The experiments presented here demonstrate that **2** rapidly activate H_2O_2 under ambient reaction conditions to catalyze the oxidation of water soluble organic dyes and paper pulp effluent. Moreover, this catalyst can be utilized in the synthesis of small N-oxides from their corresponding organic tertiary amines. Indeed, in many instances the synthesis of N-oxides proceeded with a high turnover number and high yield. These observations attest to the superior catalytic properties of this complex and its chemical versatility. While several attempts to crystallographically characterize **2** were made, results obtained from EPR spectroscopy suggest this complex has a tendency to form molecular aggregates. This

property appears to be highly solvent dependent and may inhibit homogenous crystallization.

One of the major advantages of using **2** is simple and economic synthesis of the ligand (**1**) of the complex compared to the conventional tetraamido macrocyclic ligands. Although **2** is soluble in water and rapidly activates H₂O₂ for bleaching, the activity of the complex is low compared to conventional Fe-complexes of the tetraamido macrocyclic ligands. However, **2** was used to synthesize small molecules such as N-oxides, which has never been attempted using other Fe-complexes of tetraamido macrocyclic ligands. This certainly opens new direction for further investigations. Hydrolytic stability of the complex **2** compared to the similar Fe-complexes at high temperature is low but the complex is safe to use at room temperature or slightly higher ranges. Future work will also focus on the development of additional catalysts with increased thermodynamic stability and improved catalytic activity for benign oxidations.

Acknowledgements

We thank the department of Chemistry (and Biochemistry) at UALR and UTA, respectively for financial assistance (AG and BSP). AG also likes to thank Department of Energy (Grant number DE-FG36-06G086072) for financial assistance to complete the work too.

Appendix A. Supplementary data

Supplementary data associated with this article can be found, in the online version, at doi:10.1016/j.cplett.2010.09.002.

References

- [1] R. Hage, A. Lienke, *Angew. Chem. Int. Ed.* 45 (2006) 206.
- [2] C.W. Jones, *Applications of Hydrogen Peroxide and Derivatives*, The Royal Society of Chemistry, Cambridge, 1999.
- [3] T.J. Collins, *Acc. Chem. Res.* 27 (1994) 279.
- [4] B. Meunier, J. Bernadou, *Struct. Bonding* 97 (2000) 1.
- [5] M. Costas, M.P. Mehn, M.P. Jensen, L.J. Que, *Chem. Rev.* 104 (2004) 939.
- [6] M. Sono, M.P. Roach, E.D. Coulter, J.H. Dawson, *Chem. Rev.* 96 (1996) 2841.
- [7] E.Y. Tshuva, S.J. Lippard, *Chem. Rev.* 104 (2004) 987.
- [8] T. Funabiki, in: L.I. Simandi (Ed.), *Catalysis by Metal Complexes (Advances in Catalytic Activation of Dioxygen by Metal Complexes)*, Kluwer Academic Publishers., Dordrecht/Boston/London, 2003, pp. 157–226. vol. 26.
- [9] K. Wieghardt et al., *J. Am. Chem. Soc.* 110 (1988) 7398.
- [10] M.C. White, A.G. Doyle, E.N. Jacobsen, *J. Am. Chem. Soc.* 123 (2001) 7194.
- [11] G. Yin et al., *Inorg. Chem.* 45 (2006) 3467.
- [12] G. Roelfes, M. Lubben, R.A. Hage Jr., L. Que, B.L. Feringa, *Chem. Eur. J.* 6 (2000) 2152.
- [13] G. Yin et al., *J. Am. Chem. Soc.* 127 (2005) 171170.
- [14] F.A. Chavez, P.K. Mascharak, *Acc. Chem. Res.* 33 (2000) 539.
- [15] A. Ghosh et al., *J. Am. Chem. Soc.* 127 (2005) 2505.
- [16] C.E. MacBeth, A.P. Golombek, V.G. Young Jr., C. Yang, K. Kuczera, M.P. Hendrich, A.S. Borovik, *Science* 289 (2000) 938.
- [17] T.J. Collins, *Acc. Chem. Res.* 35 (2002) 782.
- [18] W.C. Ellis, C.T. Tran, M.A. Denardo, A. Fischer, A.D. Ryabov, T.J. Collins, *J. Am. Chem. Soc.* 131 (2009) 18052.
- [19] A. Ghosh et al., *J. Am. Chem. Soc.* 302 (2003) 359.
- [20] A. Ghosh et al., *J. Am. Chem. Soc.* 130 (2008) 15116.
- [21] R. Miao et al., *Biochemistry* 47 (2008) 9888.
- [22] E. Wajnberg, L.J. El-Jaick, M.P. Linhares, D.M. Esquivel, *J. Magn. Reson.* 153 (2001) 69.
- [23] T.G. St Pierre, P. Chan, K.R. Bauchspiess, J. Webb, S. Betteridge, S. Walton, D.P.E. Dickson, *Coord. Chem. Rev.* 151 (1996) 125.
- [24] E.A. Zhilinskaya, G. Delahay, M. Mauvezin, B. Coq, A. Aboukais, *Langmuir* 19 (2003) 3596.
- [25] R.S. Drago, *Physical Methods in Chemistry*, Saunders, 1992.
- [26] H. Rupp, K.K. Rao, D.O. Hall, R. Cammack, *Biochim. Biophys. Acta.* 537 (1978) 255.
- [27] M.W. Makinen, M.B. Yim, *Proc. Natl. Acad. Sci. USA* 78 (1981) 6221.
- [28] M. Sahlén, A. Gräslund, A. Ehrenberg, *J. Magn. Reson.* 67 (1986) 135.
- [29] A. Davydov, A. Liu, A. Gräslund, *J. Inorg. Biochem.* 80 (2000) 213.
- [30] C.P. Horwitz, D.R. Fooksman, L.D. Vuocolo, S.W. Gordon-Wylie, N.J. Cox, T.J. Collins, *J. Am. Chem. Soc.* 120 (1998) 4867.
- [31] C.P. Horwitz et al., *ACS Symp. Ser.* 921 (2006) 156.
- [32] A. Albini, *Synthesis* (1993) 263.
- [33] A. Albini, S. Pietra, *Heterocyclic N-oxides*, CRC Press, Boca Raton, 1991.
- [34] E. Ember, S. Rothbart, R. Puchta, R. van Eldik, *New J. Chem.* 33 (2009) 34.